

## Crystallization of optically thick films of $\text{Co}_x\text{Fe}_{80-x}\text{B}_{20}$ : Evolution of optical, magneto-optical, and structural properties

Apoorva Sharma <sup>1</sup>, Maria A. Hoffmann <sup>2</sup>, Patrick Matthes <sup>3</sup>, Olav Hellwig <sup>1,4</sup>, Cornelia Kowol,<sup>2</sup> Stefan E. Schulz,<sup>2,3</sup> Dietrich R. T. Zahn <sup>1</sup> and Georgeta Salvan <sup>1</sup>

<sup>1</sup>*Institute of Physics, Chemnitz University of Technology, 09126 Chemnitz, Germany*

<sup>2</sup>*Center for Microtechnologies, Chemnitz University of Technology, 09126 Chemnitz, Germany*

<sup>3</sup>*Fraunhofer Institute for Electronic Nanosystems, 09126 Chemnitz, Germany*

<sup>4</sup>*Institute of Ion Beam Physics and Materials Research, Helmholtz-Zentrum Dresden-Rossendorf, 01328 Dresden, Germany*



(Received 10 October 2019; accepted 24 December 2019; published 26 February 2020)

CoFeB alloys are highly relevant materials for spintronic applications. In this work, the crystallization of CoFeB alloys triggered by thermal annealing was investigated by x-ray diffraction techniques and scanning electron microscopy, as well as spectroscopic ellipsometry and magneto-optical Kerr effect spectroscopy for annealing temperatures ranging from 300 to 600°C. The transformation of  $\sim 100$ -nm-thick  $\text{Co}_x\text{Fe}_{(80-x)}\text{B}_{20}$  films from amorphous to polycrystalline was revealed by the sharpening of spectral features observed in optical and magneto-optical dielectric functions spectra. The influence of B on the dielectric function was assessed both experimentally and by optical modeling. By analyzing the Drude component of the optical dielectric function, a consistent trend between the charge-carrier scattering time/resistivity and the annealing temperature was observed, in agreement with the electrical investigations by means of the four-point-probe method.

DOI: [10.1103/PhysRevB.101.054438](https://doi.org/10.1103/PhysRevB.101.054438)

### I. INTRODUCTION

In the last few decades,  $3d$  transition-metal borides have gained considerable interest due to their highly customizable mechanical, electrical, thermal, and magnetic properties compared to generic  $3d$  transition metals and alloys [1–3]. One of such  $3d$  transition-metal borides is CoFeB, which has received special attention not only from the fundamental research point of view, but also in industrial applications [4–6]. The increasing interest in CoFeB alloys relates to their atypical properties, such as structurally smooth growth [7], soft magnetic properties [8], high spin polarization [9], and very low Gilbert damping [10], which makes them especially suitable for magnetic tunnel junction devices [8–11]. By exploiting the benefits mentioned above, Ikeda *et al.* in the year 2005 presented a milestone improvement in the tunnel magnetoresistance ratio (TMR) in  $\text{Co}_{40}\text{Fe}_{40}\text{B}_{20}/\text{MgO}/\text{Co}_{40}\text{Fe}_{40}\text{B}_{20}$  magnetic tunnel junction of 355% at room temperature (RT) [12]. The improved TMR ratio was ascribed to the improvement in the texture of the MgO barrier due to the CoFeB electrodes. In the same year, Djayaprawira *et al.* reported that a 20% inclusion of B in the CoFe maintains it amorphous during the deposition, thereby preventing any lattice mismatch issues at the interface with MgO [7]. This allows using thin MgO grown with a well-defined (001) texture as a template for the CoFeB crystallization induced by a postdeposition thermal treatment. In 2008, a TMR ratio of  $\sim 600\%$  at RT was reported in  $\text{Co}_{20}\text{Fe}_{60}\text{B}_{20}/\text{MgO}/\text{Co}_{20}\text{Fe}_{60}\text{B}_{20}$  annealed at 525°C [13]. On the other hand, it has also been observed that annealing at higher temperature could induce interlayer diffusion [14], resulting in a degradation of the TMR ratio. Therefore, it is important to understand the influence of temperature and

composition on the crystallization of  $\text{Co}_x\text{Fe}_{(80-x)}\text{B}_{20}$  alloys in detail. Previous studies mainly focused on assessing the crystallization of CoFeB alloys using x-ray diffractometry (XRD) [15], transmission electron microscopy (TEM) [16], resistivity [3,17], magnetoresistance [18], and magnetometry measurements [19]. However, these techniques inherit some limitations, regarding the sample volume required for obtaining a reliable signal (e.g., XRD), are invasive (TEM), require complex microfabrication processes for realizing devices (magnetoresistance measurements), or provide only an indirect indication of the crystallization (electrical and magnetic measurements).

In this work, we propose a nondestructive, high-precision, swift, and highly sensitive approach to probe the crystallization of  $\text{Co}_x\text{Fe}_{(80-x)}\text{B}_{20}$  based on spectroscopic ellipsometry (SE) and magneto-optical Kerr effect (MOKE) spectroscopy. Spectroscopic ellipsometry has proven to be a very sensitive method for investigating thin films [20], also providing the possibility of probing changes in the crystalline structure, as investigated for Si [21], diblock polymers [22], or organic photovoltaic devices [23]. Similar to SE, MOKE spectroscopy has also demonstrated its efficacy in probing not only the structural changes, but also as being a highly sensitive tool to investigate the local environment effects. For instance, Bräuer *et al.* showed that MOKE spectroscopy can be used as a suitable method to determine the orientation of metal-free phthalocyanine molecules on various substrates [24]. Furthermore, the systematic study by Tikuišis *et al.* on a permalloy film shows that the MOKE spectroscopy and the magneto-optical dielectric function are strongly influenced by surface oxidation [25], thus revealing a superior sensitivity of the MOKE spectroscopy to the changes in the surrounding of

the ferromagnetic material. So far, only few studies addressed the optical and magneto-optical properties of CoFe alloys [26–28] or CoFeB [29,30]. In a recent study, we reported on the sensitivity of SE and MOKE spectroscopy with respect to the crystallization of thin films of  $\text{Co}_{60}\text{Fe}_{20}\text{B}_{20}$  [31]. Here, we exploit this sensitivity to extract information related to the influence of the B content in the amorphous alloys on the crystallization process. In addition, we demonstrate that the Drude contribution to the dielectric functions and the corresponding parameters (resistivity and scattering time) is susceptible to the crystallization onset.

## II. METHODS

### A. Structural and electrical investigations

Magnetron sputtering was used to deposit 100-nm-thick  $\text{Co}_x\text{Fe}_{(80-x)}\text{B}_{20}$  films with  $x = 40$  and  $60$ , as well as  $\text{Co}_{50}\text{Fe}_{50}$ , from composite targets on silicon wafers with native silicon oxide. The layers were passivated with 5 nm of Pt to prevent oxidation of the CoFeB. The deposition was performed at RT with a base pressure below  $2 \times 10^{-4}$  Pa and Ar working pressure of 0.35 Pa. The wafers were diced in  $1 \text{ cm} \times 1 \text{ cm}$  pieces, and each individual piece was then annealed for 30 min at temperatures in the range of 300 to 600°C in steps of 50 K in an high vacuum (HV) ( $10^{-5}$  Pa) oven. To improve thermal conductivity between the heater and sample a thin layer of silver epoxy was used. The samples were investigated *ex situ* after each annealing step. The  $\text{Co}_{50}\text{Fe}_{50}$  sample served as a standard, and no further annealing was performed.

XRD measurements were conducted using a SmartLab diffractometer from Rigaku, equipped with a rotating Cu anode operated at 9 kW. XRD in  $\theta$ - $2\theta$  geometry, grazing-incidence XRD (GIXRD), and x-ray reflectometry (XRR) measurements were performed to probe the crystallization, crystallite size, and thickness of the films while always using a parallel beam. The crystallite size ( $L$ ) was calculated using the Scherrer formula

$$L \approx \frac{K\lambda_{\text{Cu}}}{\Delta(2\theta)\cos\theta}, \quad (1)$$

with a shape factor of crystallites  $K \approx 0.9$  considering cubic crystallites, the wavelength of x-ray radiation  $\lambda_{\text{Cu}} \approx 0.154 \text{ nm}$ , and  $\Delta(2\theta)$  as the full width at half maximum (FWHM) of the reflex at  $\theta$ , given in radians [32].

The information about the thickness of the layers was extracted from simulating the reflectance scans using GENX [33]. The thickness values obtained from XRR of  $\text{Co}_{50}\text{Fe}_{50}$ ,  $\text{Co}_{40}\text{Fe}_{40}\text{B}_{20}$ ,  $\text{Co}_{60}\text{Fe}_{20}\text{B}_{20}$ , and Pt of as-deposited samples are shown in Table I. The cross-sectional morphologies of

TABLE I. XRR-determined thickness of the  $\text{Co}_x\text{Fe}_{(80-x)}\text{B}_{20}$ ,  $\text{Co}_{50}\text{Fe}_{50}$ , and Pt layers for the as-deposited samples.

Sample ID	Thickness	
	$t_{\text{CoFeB}}$ (nm)	$t_{\text{Pt}}$ (nm)
$\text{Co}_{50}\text{Fe}_{50}$	$61.5 \pm 1$	$3.64 \pm 1$
$\text{Co}_{40}\text{Fe}_{40}\text{B}_{20}$	$97.4 \pm 5$	$4.78 \pm 1$
$\text{Co}_{60}\text{Fe}_{20}\text{B}_{20}$	$104.6 \pm 5$	$4.81 \pm 1$

the  $\text{Co}_x\text{Fe}_{(80-x)}\text{B}_{20}$  films were inspected using an Auriga 60 scanning electron microscope (SEM) from Zeiss equipped with a focused ion beam (FIB). The surface of the samples was studied by atomic force microscopy (AFM) in AC mode with an Agilent 5500 Scanning Probe Microscope, using reflective Si AFM probes.

The sheet resistance of all samples annealed at different temperatures was measured with the four-point probe technique using a home-built test bench, consisting of four gold-coated copper probes arranged in an equally spaced ( $d \sim 1 \text{ mm}$ ) collinear manner.

### B. (Magneto-)optical methods and modeling

Spectroscopic ellipsometry measurements were performed using an M-2000 ellipsometer from J. A. Woollam over the spectral range of 0.7 to 5 eV, with varying angles of incidence, in the range of  $45^\circ$ – $75^\circ$  in steps of  $5^\circ$ . In order to determine the dielectric function ( $\epsilon_{xx} = \epsilon_{1,xx} + i\epsilon_{2,xx}$ ) of CoFeB from the measured  $\Psi$  and  $\Delta$  spectra, an optical model analogous to the physical layer structure was devised in the modeling and simulation tool CompleteEASE®. Thus, a “Si/SiO<sub>2</sub>(1.8 nm)/CoFeB( $t_{\text{CoFeB}}$ )/Pt( $t_{\text{Pt}}$ )/ surface roughness” layered optical model was built using the reported dielectric function of Si [34], SiO<sub>2</sub> [34], and Pt [35] layers. Additionally, the layer thicknesses determined by XRR and the surface roughness determined by AFM were used in the optical model and were kept unchanged throughout the analysis. The unknown dielectric function of CoFeB was expressed in terms of the Lorentz-Drude model [Eq. (2)] [36]. This model is composed of a Drude function to account for the free-charge-carrier contribution and two Lorentzian oscillators to describe the dispersion arising from interband transitions. This model was further adjusted in terms of the Drude and Lorentzian parameters to respond to the structural changes resulting from the annealing.

$$\epsilon(E) = \epsilon_{\text{Drude}} + \epsilon_{\text{Lorentz}}, \quad (2)$$

where  $\epsilon(E)$  is the complex dielectric function,  $E$  is the photon energy,  $\epsilon_{\text{Drude}}$  and  $\epsilon_{\text{Lorentz}}$  are the Drude and Lorentzian contribution to the dielectric spectrum.

The version of the Lorentzian oscillator used here is a mathematical equation based on the Newton equation of motion that defines the influence of the electric field on the bound electrons.

$$\epsilon_{\text{Lorentz}}(E) = \frac{A\gamma E_o}{E_o^2 - E^2 - iE\gamma}, \quad (3)$$

where  $A$ ,  $\gamma$ , and  $E_o$  are the amplitude, the FWHM, and the center energy position of the oscillator, respectively.

The classical Drude equation defines the free-charge-carrier concentration contribution to the dielectric function, which in its mathematical form is equivalent to a Lorentzian oscillator positioned at 0 eV:

$$\epsilon(E) = \frac{-\hbar}{\epsilon_0\rho(\tau_s E^2 + i\hbar E)}, \quad (4)$$

where  $\epsilon_0$  is the vacuum dielectric constant,  $\hbar$  is the reduced Planck constant,  $\tau_s$  is the mean scattering time of the free carriers between successive collisions and  $\rho$  is the resistivity.

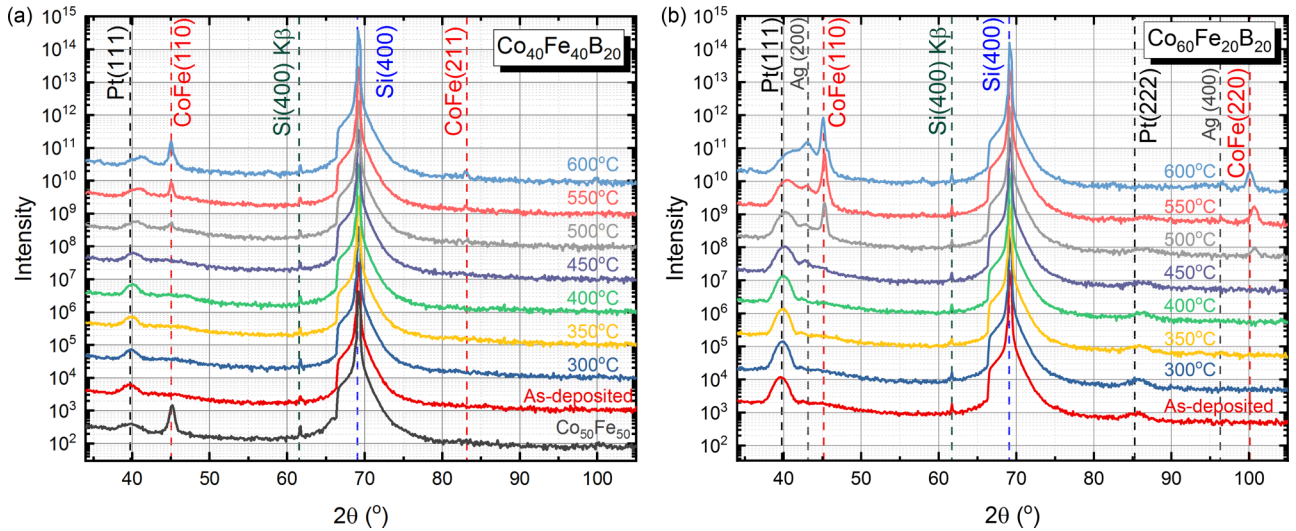


FIG. 1. X-ray diffraction patterns recorded for substrate/ $\text{Co}_x\text{Fe}_{(80-x)}\text{B}_{20}/\text{Pt}$  before and after annealing at the indicated temperatures for (a)  $x = 40\%$  and (b)  $x = 60\%$ . Additionally, the scan of the as-deposited  $\text{Co}_{50}\text{Fe}_{50}/\text{Pt}$  sample is presented in black in (a) for reference. The respective reflexes of the constituent materials are marked by dashed lines along with the respective Miller indices.

A home-built MOKE spectrometer in polar geometry (pMOKE) was utilized to measure the photon energy-dependent Kerr rotation ( $\theta_K$ ) and ellipticity ( $\eta_K$ ) [37]. Both  $\theta_K(E)$  and  $\eta_K(E)$  were recorded with an out-of-plane applied magnetic field of  $H \sim 1.8$  T. By magnetizing the layers normal to the sample surface and assuming optical isotropy of the studied CoFeB alloys, the dielectric tensor can be formulated as

$$\varepsilon = \begin{pmatrix} \varepsilon_{xx} & \varepsilon_{xy} & 0 \\ -\varepsilon_{xy} & \varepsilon_{xx} & 0 \\ 0 & 0 & \varepsilon_{zz} \end{pmatrix}. \quad (5)$$

The diagonal components of the dielectric tensor ( $\varepsilon_{xx}$ ) are obtained from the SE measurements, while the off-diagonal component ( $\varepsilon_{xy} = \varepsilon_{1xy} + i\varepsilon_{2xy}$ ), reflecting the magneto-optical response of the films, are calculated from the recorded  $\theta_K$  and  $\eta_K$ , using a point-by-point fitting method described elsewhere [38], considering the same optical layer model as used in SE.

### III. RESULTS AND DISCUSSION

#### A. X-ray diffractometry

Figure 1 presents the XRD  $\theta$ - $2\theta$  scans of the CoFeB samples annealed in vacuum at different temperatures. The pronounced CoFe(110) reflex observed at 500°C and above indicates crystallization of the films. In accordance with previous studies, the creation of a crystalline alloy from the initial CoFeB compound occurs while boron diffuses out of the lattice resulting in pure CoFe crystals surrounded by amorphous boron [39,40]. Furthermore, a closer look at the diffractograms indicates that  $\text{Co}_{40}\text{Fe}_{40}\text{B}_{20}$  crystallizes in a polycrystalline fashion, as the present (110) and (211) peaks correspond to different crystallographic orientations of body-centered cubic (bcc) CoFe.  $\text{Co}_{60}\text{Fe}_{20}\text{B}_{20}$ , on the other hand, reveals a strong (110) texture, with more intense (110) and (220) peaks occurring. The strong (110) texture was also

confirmed by additional rocking-scan analysis of the (110) out-of-plane crystallite orientation distribution (see the following discussion). At temperatures above 550°C, a shift and broadening of the Pt(111) peak are found for both stoichiometries, most probably suggesting a degradation of the Pt layer, possibly due to alloying or intermixing at the interface with CoFeB. Here, it is worth mentioning that three stray reflexes at 61°, 43°, and 97° are from silicon (400) due to Cu- $K_\beta$  radiation, and Ag(200) as well as Ag(400) from silver epoxy, respectively.

The vertical coherence lengths, corresponding to the crystallite size ( $L$ ) in the normal direction to the sample surfaces, were calculated from the FWHM of the  $\text{Co}_{50}\text{Fe}_{50}$ (110) peak. For the investigated films, a maximum crystallite size of around  $(25 \pm 2)$  nm is obtained for annealing temperatures of 600°C, as shown in Fig. 2(a), which is consistent with previously reported studies on 100 nm thick CoFeB films [16]. As detected by cross-section scanning electron microscopy studies [see Fig. 2(b)], the CoFe alloy does not fully crystallize within the 30 min applied annealing steps. The crystallization starts from the top interface with Pt and expands for 25–30 nm, in agreement with the vertical coherence length of the crystallites determined from XRD.

The observation of a distinct out-of-plane (110) texture formation for the  $\text{Co}_{60}\text{Fe}_{20}\text{B}_{20}$  film in the Bragg scans of Fig. 1 is further confirmed and supported by additional rocking scans (Omega scans) that directly reveal the actual crystallite orientation distribution. Figure 3 shows the rocking scan profiles for the  $\text{Co}_{60}\text{Fe}_{20}\text{B}_{20}$  film, which exhibit a clear preferred out-of-plane (110) texture formation, once annealed to 500°C. The transition from the polycrystalline structure to the (110) textured structure occurs very suddenly, as confirmed by the dramatic shape change of the rocking-scan profile from 450 to 500°C. After an initial FWHM of about 12° after annealing to 500°C the (110) crystallite out-of-plane alignment improves further to a FWHM of below 9° after annealing to 600°C. In contrast to this strong texture formation of the  $\text{Co}_{60}\text{Fe}_{20}\text{B}_{20}$  film above 450°C, the  $\text{Co}_{40}\text{Fe}_{40}\text{B}_{20}$  film reveals the same

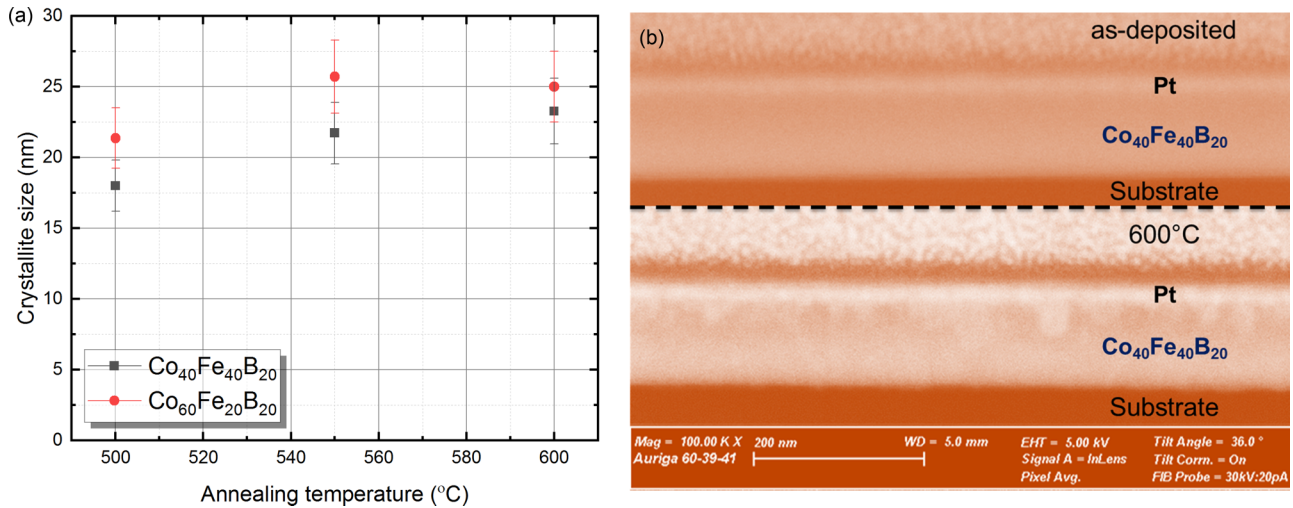


FIG. 2. (a)  $\text{Co}_{50}\text{Fe}_{50}$  crystallite sizes normal to the film plane calculated using the Scherrer expression for  $\text{Co}_{40}\text{Fe}_{40}\text{B}_{20}$  and  $\text{Co}_{60}\text{Fe}_{20}\text{B}_{20}$  and the XRD patterns shown in Fig. 1. (b) SEM micrograph collage of substrate/ $\text{Co}_{40}\text{Fe}_{40}\text{B}_{20}$ /Pt before and after annealing recorded in the FIB trench at  $36^\circ$  stage tilt.

polycrystalline rocking-scan characteristics for all annealing temperatures (not shown here). Only an overall strong increase in the rocking-scan intensity above  $450^\circ\text{C}$  also confirms for the  $\text{Co}_{40}\text{Fe}_{40}\text{B}_{20}$  film an increased coherence length, i.e., increased size of the randomly oriented crystallites.

To investigate near-surface changes in the layer and to avoid the intense peak from the silicon substrate, GIXRD was performed. The differences in the crystallization of both CoFeB compositions become even more pronounced after the analysis of GIXRD scans at fixed  $\Omega = 1^\circ$ , shown in Fig. 4. All the aforementioned CoFe peaks are present after annealing at  $500$ ,  $550$ , and  $600^\circ\text{C}$  for  $\text{Co}_{40}\text{Fe}_{40}\text{B}_{20}$ , as well as for  $\text{Co}_{50}\text{Fe}_{50}$  in the as-deposited state [see Fig. 4(a)], confirming the polycrystalline nature of the CoFe alloy in this composition. On

the contrary, for  $\text{Co}_{60}\text{Fe}_{20}\text{B}_{20}$  shown in Fig. 4(b), none of the CoFe peaks are detected as the film is well (110) textured and thus the Bragg condition for CoFe crystallites is not fulfilled for any detector angle due to the fixed incident angle of  $\Omega = 1^\circ$  and  $\chi = \varphi = 0^\circ$ . The Pt passivation layer deposited on the top of  $\text{Co}_{40}\text{Fe}_{40}\text{B}_{20}$  layer exhibits polycrystallinity even at the highest annealing temperature, whereas the Pt layer on top of  $\text{Co}_{60}\text{Fe}_{20}\text{B}_{20}$  was noticed to transform to (200) texture upon annealing.

## B. Spectroscopic ellipsometry

Using the optical model discussed in the experimental section, the complex dielectric functions ( $\epsilon_{1xx}$  and  $\epsilon_{2xx}$ ) were determined for the two investigated CoFeB stoichiometries and  $\text{Co}_{50}\text{Fe}_{50}$ . For the ease of discussion, the spectra can be divided into two main regions: (i) the near-infrared (NIR) region below  $1.0$  eV, accounting for intraband transitions, and (ii) the visible and ultraviolet (UV) region above  $1.0$  eV, related mainly to interband contributions. The NIR region of the spectrum is described by a Drude-type contribution, related to the free-electron absorption in  $\text{Co}_{50}\text{Fe}_{50}$ , and will be discussed in more detail in the following.

In the case of  $\text{Co}_{50}\text{Fe}_{50}$ , the Drude contribution is followed by a broad structure centered at around  $\sim 1.5$  eV in the  $\epsilon_{1xx}$  spectra (corresponding feature at  $\sim 2$  eV in  $\epsilon_{2xx}$  spectra (see Fig. 5). This feature was previously ascribed to the hybridization of  $p$  and  $d$  orbitals, resulting in direct interband transitions from occupied  $d$  to unoccupied  $p$  states in CoFe alloys with a bcc crystalline phase [26,28].

In order to understand the influence of B inclusions on the optical properties of the  $\text{Co}_{50}\text{Fe}_{50}$ , the complex dielectric function of  $(\text{Co}_{50}\text{Fe}_{50}) + \text{B}$  was simulated. For this purpose, the Bruggemann effective medium approximation approach was used to calculate the optical constants of the mixed material with the host matrix of  $\text{Co}_{50}\text{Fe}_{50}$  with B inclusion. In this approach, 15% of the  $(\text{Co}_{50}\text{Fe}_{50}) + \text{B}$  film volume is assumed to be a spherical inclusion of B in the metallic  $\text{Co}_{50}\text{Fe}_{50}$ . However, it should be noted that this is only a

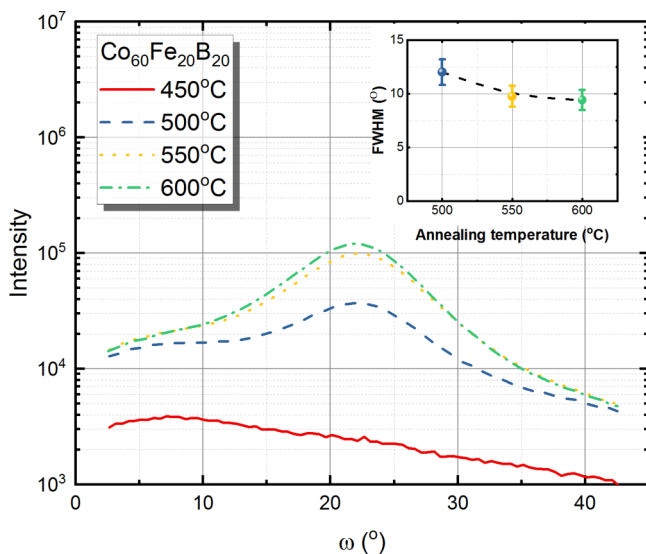


FIG. 3. Omega scans (rocking curve) measured at the  $\text{Co}_{50}\text{Fe}_{50}(110)$  reflex for the  $\text{Co}_{60}\text{Fe}_{20}\text{B}_{20}$ . The inset shows the FWHM determined by using a Gaussian fit to the measured rocking-scan profiles.

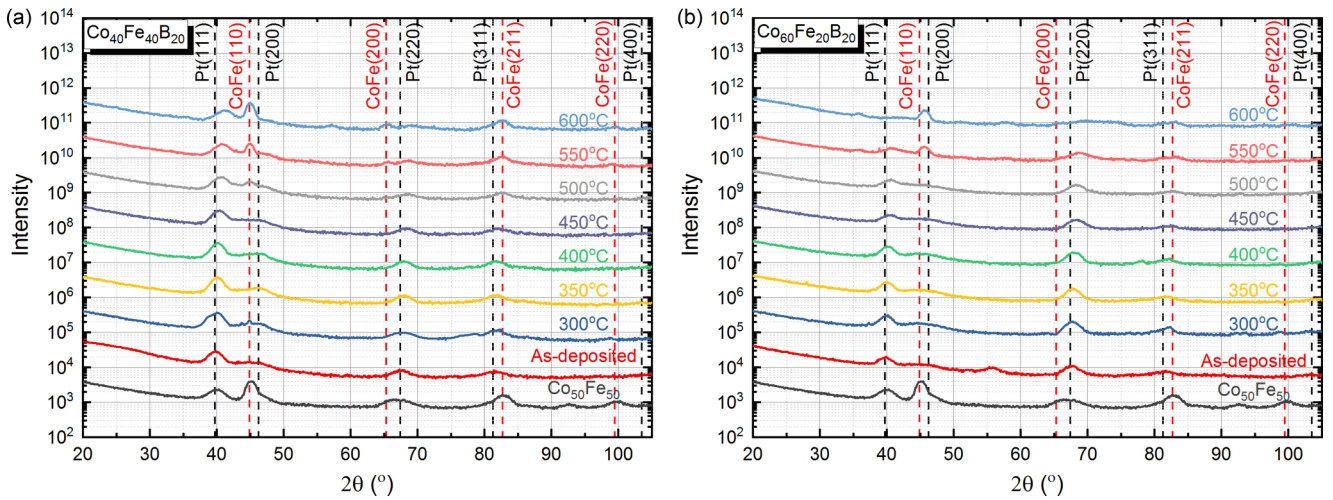


FIG. 4. GIXRD scans at  $\Omega = 1^\circ$  recorded before and after annealing at various temperatures for (a)  $\text{Co}_{40}\text{Fe}_{40}\text{B}_{20}$  and (b)  $\text{Co}_{60}\text{Fe}_{20}\text{B}_{20}$ . The expected positions of the XRD peaks are marked by the dotted lines along with the respective Miller indices.

coarse approximation of the actual situation; previous studies suggested that B migrates to CoFe grain boundaries or to the neighboring layers [39,40]. The most obvious change induced to the dielectric function spectra of  $\text{Co}_{50}\text{Fe}_{50}$  by the B inclusion is visible in the  $\varepsilon_{2xx}$  spectrum, namely a decrease of the absolute values. Since B is a nonmetallic material, its addition to the metallic  $\text{Co}_{50}\text{Fe}_{50}$  increases the dielectric losses. Consistently, the values of  $\varepsilon_{1xx}$  increase, indicating an increase in the relative permittivity of CoFeB. A slight broadening of the spectral features is also observed, but rather negligible when compared with the changes in the features of the dielectric functions of the CoFeB alloys extracted from the experimental ellipsometry spectra before and after annealing (see Fig. 6). The good correspondence between the simulated complex dielectric function of B incorporated in CoFe and the dielectric function determined for the  $\text{Co}_{40}\text{Fe}_{40}\text{B}_{20}$  indicates that during the crystallization process CoFe crystallites are

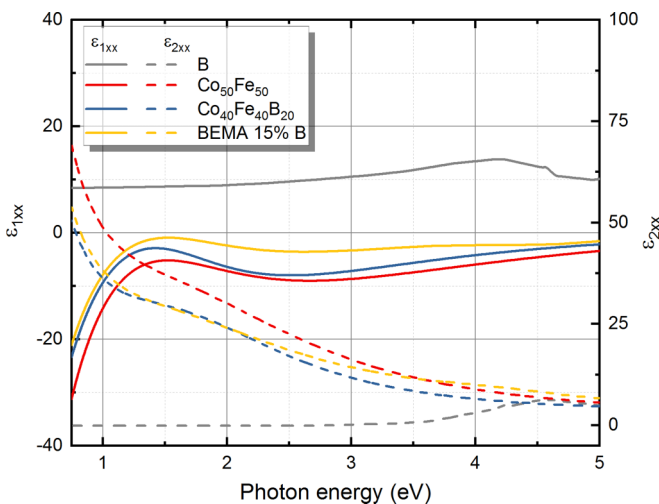


FIG. 5. The complex dielectric function ( $\varepsilon_{1xx}$  and  $\varepsilon_{2xx}$ ) spectra of the  $\text{Co}_{50}\text{Fe}_{50}$  (red),  $\text{Co}_{40}\text{Fe}_{40}\text{B}_{20}$  (blue) annealed at  $600^\circ\text{C}$  and B (gray) [42], together with the simulated  $\varepsilon_{1xx}$  and  $\varepsilon_{2xx}$  of  $(\text{Co}_{50}\text{Fe}_{50}) + \text{B}$  with 15% B content (yellow).

formed and B migrates outside the crystallites, i.e., to the grain boundaries. This scenario is in line with the results of previous studies of the local structure of CoFeB [39] and for crystalline CoCrPt-B alloys used for recording media in hard-disk drives [41].

The dielectric functions of the as-deposited CoFeB alloys present only weak and very broad spectral features, which gradually become more pronounced with an increase in annealing temperature, as shown in Fig. 6. The characteristic spectral feature of  $\text{Co}_{50}\text{Fe}_{50}$  at  $\sim 1.5$  eV occurs in the  $\varepsilon_{1xx}$  spectra for the samples annealed at  $450^\circ\text{C}$ . This suggests that  $450^\circ\text{C}$  is the onset temperature for crystallization. As the optical spectroscopy has an information depth limited to a few 10 nm, the changes visible in the spectra at  $450^\circ\text{C}$  indicate that the crystallization takes place near the surface ( $\text{Co}_x\text{Fe}_{(80-x)}\text{B}_{20}/\text{Pt}$  interface), as supported by scanning electron microscopy images [cf. Fig. 2(b)] demonstrating a nucleation at the Pt interface. Noticeably, the pronounced CoFe reflex was observed in XRD scans starting at  $500^\circ\text{C}$ , indicating that the optical spectroscopy allows probing the incipient phase of crystallization with very small crystallites. In fact, a remarkable resemblance of the dielectric function of the  $\text{Co}_{40}\text{Fe}_{40}\text{B}_{20}$  after annealing at  $600^\circ\text{C}$  and the as-deposited  $\text{Co}_{50}\text{Fe}_{50}$  is found, which is consistent with the similarities in the crystalline structure observed with XRD. This suggests that at  $600^\circ\text{C}$  B diffuses completely out of the CoFe crystallites. The systematic decrease in  $\varepsilon_{2xx}$  with annealing temperature is furthermore consistent with a greater ordering within the films due to crystallization. The characteristic spectral feature in  $\varepsilon_{1xx}$  spectra of  $\text{Co}_{60}\text{Fe}_{20}\text{B}_{20}$  is redshifted relative to  $\text{Co}_{40}\text{Fe}_{40}\text{B}_{20}$ , probably due to the difference in the stoichiometric composition. Additionally, comparing the amplitudes of the  $\varepsilon_{2xx}$  spectra (mostly  $< 1$  eV) of the two stoichiometries, it is evident that the  $\text{Co}_{40}\text{Fe}_{40}\text{B}_{20}$  has lower dielectric losses due to the free electrons in comparison to  $\text{Co}_{60}\text{Fe}_{20}\text{B}_{20}$ . This, in turn, implies that increasing Co concentration increases the charge-carrier concentration, which is consistent with the empirical finding that the resistivity of Co is almost half of that of Fe [43,44].

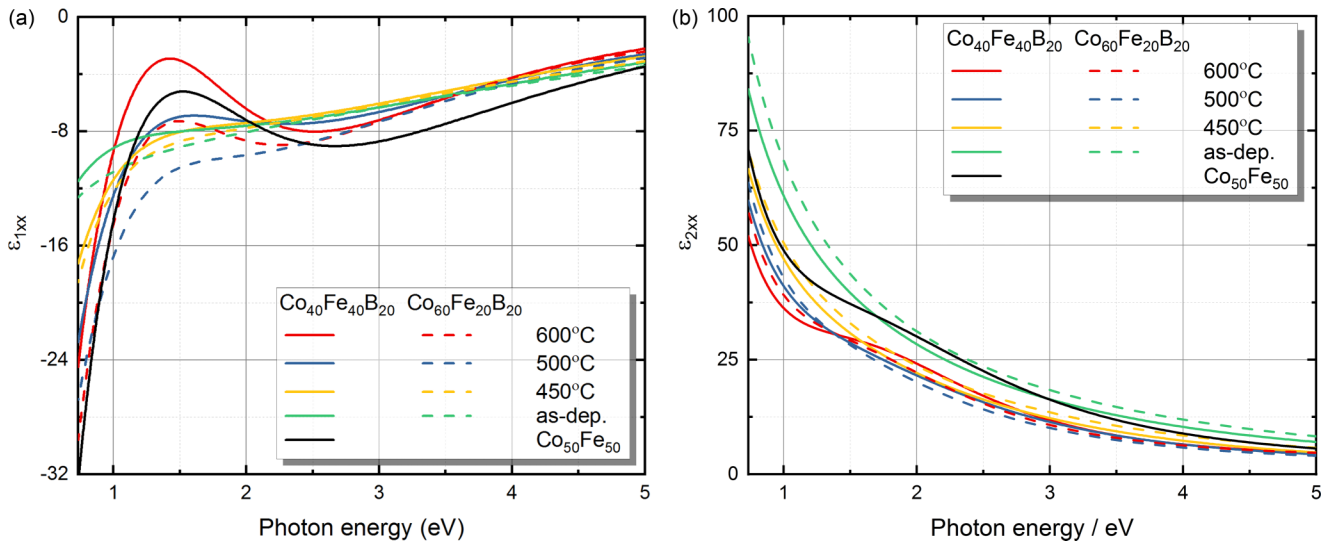


FIG. 6. Annealing temperature dependence of (a)  $\epsilon_{1xx}$  and (b)  $\epsilon_{2xx}$  spectra for  $\text{Co}_{40}\text{Fe}_{40}\text{B}_{20}$  (solid lines) and  $\text{Co}_{60}\text{Fe}_{20}\text{B}_{20}$  (dashed lines), and  $\text{Co}_{50}\text{Fe}_{50}$  (black).

The analysis of the Drude contribution to the dielectric function allows deriving the resistivity ( $\rho$ ) and scattering time ( $\tau_s$ ) of the investigated films. The resistivity and the scattering time ultimately relate to the ordering state of the films, according to the Fuchs size-effect theory [45]. These parameters are shown in Fig. 7(a) for both CoFeB stoichiometries. The resistivity remains barely unchanged until 400°C, followed by a maximum at 450°C and a subsequent decrease with increasing annealing temperature. It should be noted that this evolution cannot be explained by the B diffusion since in Ref. [14] we showed that the migration of B starts already at 200°C. The decrease in resistivity can be ascribed to an increase in ordering and decrease in the number of defects, which, in fact, is consistent with the increase in the crystallite size derived from the XRD measurements. The presence of

a maximum at 450°C relates very likely to a temperature of nucleation of the crystallites, where the electrical resistivity increases due to the formation of grain boundaries and defects, originating from the low level of ordering of the crystal. The poly-textured phase in  $\text{Co}_{40}\text{Fe}_{40}\text{B}_{20}$  (in contrast to the well-oriented phase in  $\text{Co}_{60}\text{Fe}_{20}\text{B}_{20}$ ) could arguably also explain the difference in the resistivity between the two alloys since more mismatched grain boundaries and defects would lead to higher resistivity due to the shorter mean-free path.

Sheet resistance ( $R_{\square}$ ) measurements were conducted on all the samples in order to investigate the influence of annealing on the electrical properties of the layers. The change in sheet resistance of the CoFeB samples with annealing temperature is shown in Fig. 7(b). Up to 400°C no significant

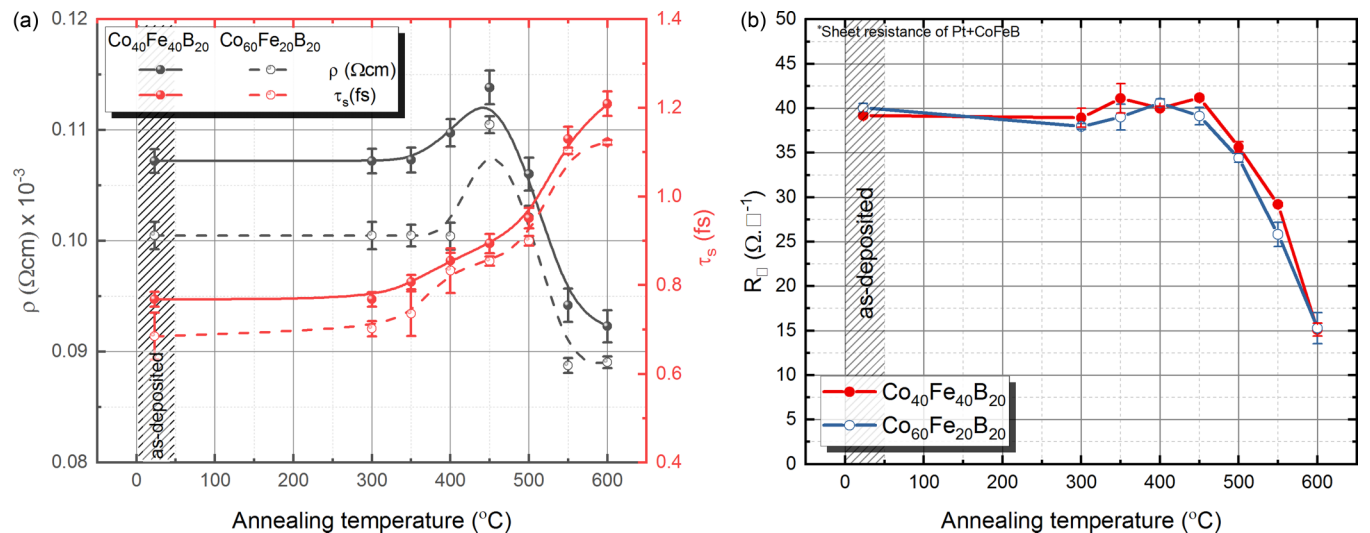


FIG. 7. (a) Drude parameters resistivity  $\rho$  and scattering time  $\tau_s$  as a function of annealing temperature for  $\text{Co}_{40}\text{Fe}_{40}\text{B}_{20}$  (solid symbol) and  $\text{Co}_{60}\text{Fe}_{20}\text{B}_{20}$  (empty symbol). The lines in the figure are guides to the eye. (b) Sheet resistance of the  $\text{Co}_{40}\text{Fe}_{40}\text{B}_{20}$  (filled circles in red) and  $\text{Co}_{60}\text{Fe}_{20}\text{B}_{20}$  (unfilled circles in blue) layers passivated with a Pt thin film as a function of the annealing temperature.

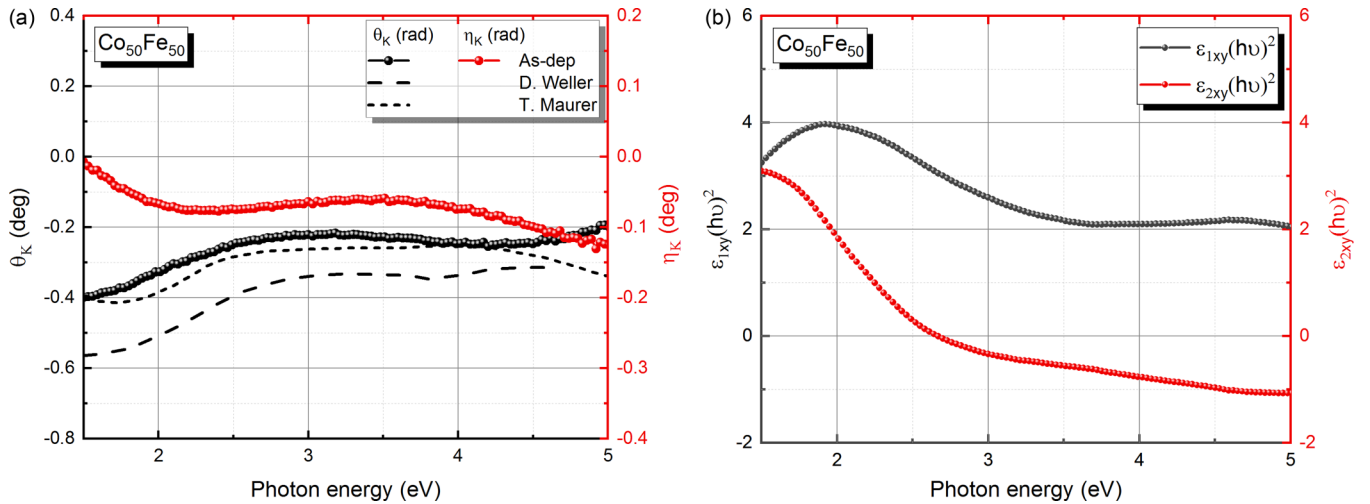


FIG. 8. Polar Kerr effect measured (a) polarization rotation ( $\theta_K$ ) and ellipticity ( $\eta_K$ ) spectra of as-deposited  $\text{Co}_{50}\text{Fe}_{50}$  in comparison to literature values [46,47] and (b) calculated  $(\hbar\nu)^2 \epsilon_{xy}$  as a function of photon energy, indicating present  $p$ - $d$  hybridization.

change in the sheet resistance is found. Above this temperature, a monotonous decrease with increasing temperature is observed, consistent with changes observed for the optical resistivity parameter calculated from the Drude model [cf. Fig. 7(a)]. Given the increase in crystallite size and ordering within the films with the annealing temperature revealed by XRD, a decrease in the scattering due to defects and grain boundaries is expected, which results in a decrease of the sheet resistance. The trend in  $R_{\square}$  for both stoichiometries is noticeably similar to the change in  $\rho$  obtained from the SE measurements.

### C. Magneto-optical spectroscopy

Figure 8(a) shows the measured  $\theta_K$  and  $\eta_K$  MOKE spectra of  $\text{Co}_{50}\text{Fe}_{50}$ , with a comparison of  $\theta_K$  reported by Weller *et al.* for  $\text{Co}_{48}\text{Fe}_{52}$  [46]. Even though the amplitude of  $\theta_K$  is

slightly lower than previously reported [46], the line shapes of both experiments resemble each other closely. In fact, the present data are closer to the first-principle calculations performed by Maurer *et al.* for this CoFe composition [47]. The off-diagonal dielectric function of  $\text{Co}_{50}\text{Fe}_{50}$  was calculated and is shown in Fig. 8(b) as  $(\hbar\nu)^2 \epsilon_{xy}$ , in order to highlight the spectral features [48]. It is well established by theoretical studies that the spin-polarized density of states of  $3d$  transition metals and their alloys are fairly similar, resulting in similar electronic transitions in magneto-optical spectra [28]. These spectral features noticed in the optical region of the spectrum can be explained based on the theoretical predictions by K. J. Kim *et al.* for  $\text{Fe}_3\text{Co}$  and  $\text{Co}_3\text{Fe}$  using the tight-binding linear-muffin-tin orbitals method with the local spin-density approximation [26,47]. They assign the transition at 2 eV as originating mainly from transitions from the occupied minority-spin  $d$  triplet states at lower energy into

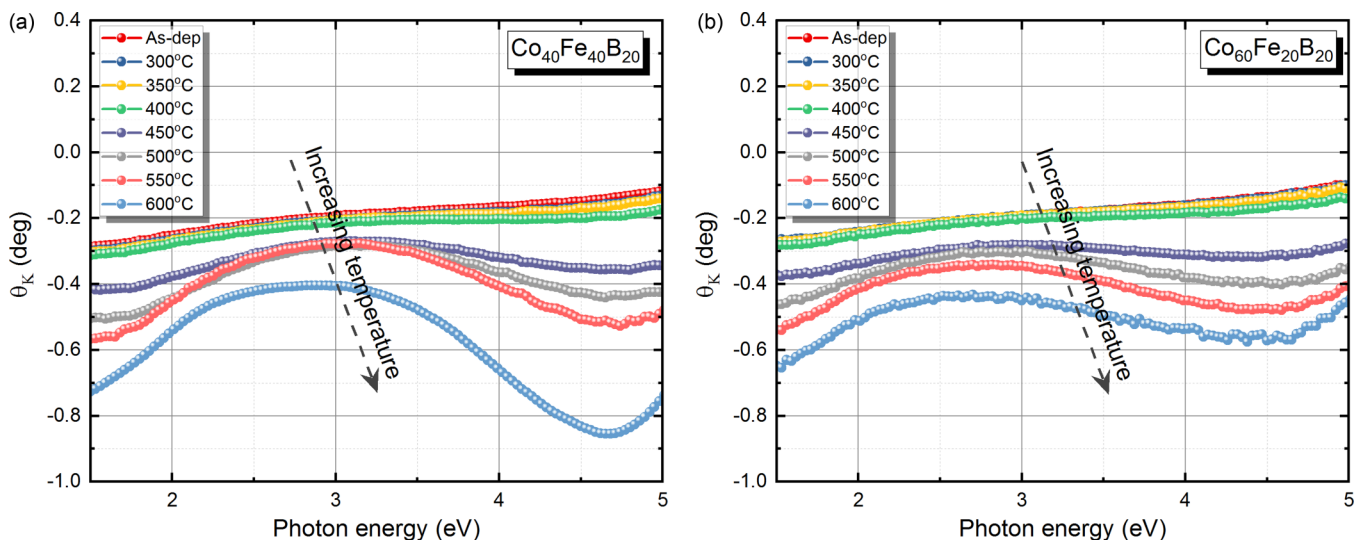


FIG. 9. Polar Kerr effect measured polarization rotation ( $\theta_K$ ) spectra for the Pt capped 100-nm-thick CoFeB film before and after annealing at various temperatures for the two stoichiometries, (a)  $\text{Co}_{40}\text{Fe}_{40}\text{B}_{20}$  and (b)  $\text{Co}_{60}\text{Fe}_{20}\text{B}_{20}$ .

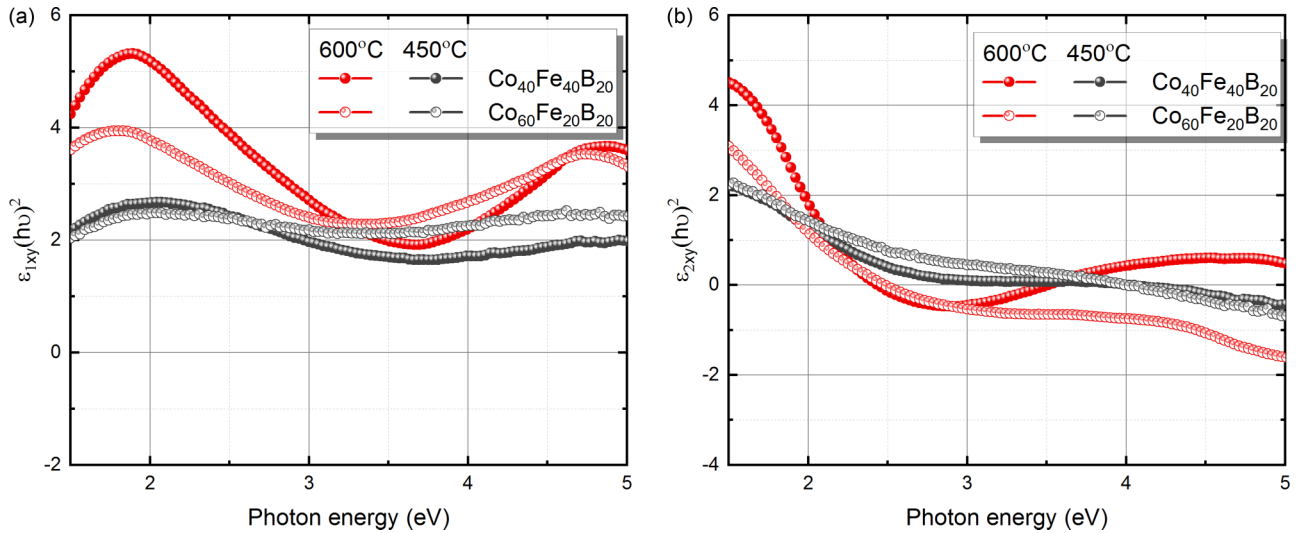


FIG. 10. Calculated  $(h\nu)^2 \varepsilon_{xy}$  as the function of photon energy for the two stoichiometry  $\text{Co}_{40}\text{Fe}_{40}\text{B}_{20}$  and  $\text{Co}_{60}\text{Fe}_{20}\text{B}_{20}$  for the samples annealed at 450 and 600°C.

the unoccupied minority-spin  $p$  states. These  $d \rightarrow p$  transitions in the minority-spin bands become possible through  $p$ - $d$  hybridization.

Figure 9 shows the evolution in  $\theta_K$  spectra for the CoFeB samples annealed at different temperatures for the investigated two stoichiometries. Similar to the SE spectra, no significant changes in  $\theta_K$  and  $\eta_K$  spectra were observed up to 400°C. Upon annealing at 450°C, the characteristic line shape of the  $\theta_K$  spectrum starts resembling that of  $\text{Co}_{50}\text{Fe}_{50}$ . Annealing at higher temperatures results in the enhancement of spectral features at  $\sim 2$  and  $\sim 4.7$  eV. This is consistent with an increasing crystalline ordering of CoFe. It can also be observed that these features are slightly redshifted for  $\text{Co}_{60}\text{Fe}_{20}\text{B}_{20}$  compared to  $\text{Co}_{40}\text{Fe}_{40}\text{B}_{20}$ , contrary to previous theoretical calculations, where no significant differences were found on the MOKE spectra of different CoFe content [28]. In fact, this shift may be as well related to the differences found by XRD in the crystalline structure of both compounds. In this context, we note that besides composition, also the crystalline environment influences the magneto-optical properties of the material significantly [49]. The larger amplitude of the spectral features of  $\text{Co}_{40}\text{Fe}_{40}\text{B}_{20}$  is, furthermore, an indication of higher magnetization for the lower Co content, which is consistent with the calculated Slater-Pauling curve [50].

The calculated  $(h\nu)^2 \varepsilon_{xy}$  as a function of the photon energy for the two CoFeB compositions annealed at 450 and 600°C is shown in Fig. 10. Similar to the off-diagonal dielectric function of  $\text{Co}_{50}\text{Fe}_{50}$ , the real part of  $\varepsilon_{xy}$  shows two main features in the measured spectral range, at  $\sim 2$  and  $\sim 4.5$  eV.

As discussed earlier, the features in the spectra reflect the density of states of the occupied part of the  $3d$  band and are ascribed to the transition to empty hybridized  $p_z$  states near the Fermi energy. The relative shifts in the positions of the spectral features of  $\text{Co}_{60}\text{Fe}_{20}\text{B}_{20}$  to lower energies with respect to the  $\text{Co}_{40}\text{Fe}_{40}\text{B}_{20}$  case indicate that the density of states strongly depends on the stoichiometry. This shift was further explained by Liu and Singh with the theoretical

calculation of the electronic structure of CoFe alloys [51]. Though the density of states near the Fermi energy is similar for both Co and Fe, due to the higher electronegativity and a smaller exchange splitting of Co, the minority-spin orbitals of Co are situated at lower energy as compared to the Fe orbitals. Hence a higher percentage of Co in the alloy will lead to a shift of the states to lower energies. The change in amplitude of the spectral features relates, as mentioned previously, to the magnetization, increasing in the case of 600°C annealing with increasing Fe content [50].

#### IV. CONCLUSION

In this work, the optical- and magneto-optical properties of optically thick (100 nm) films of  $\text{Co}_x\text{Fe}_{(80-x)}\text{B}_{20}$  ( $x = 40$  and 60%) passivated with a 5 nm Pt cap layer were investigated in the as-deposited amorphous state and upon subsequent annealing steps between 300 and 600°C. The structural and electrical properties of the films were assessed by XRD and electrical four-point probe measurements, respectively. The comparison of the  $\text{Co}_x\text{Fe}_{(80-x)}\text{B}_{20}$  dielectric function extracted from spectroscopic ellipsometry with that of  $\text{Co}_{50}\text{Fe}_{50}$  allowed us to identify CoFe specific spectral features and to analyze the impact of B on the optical properties of the CoFeB alloys.

The (magneto-)optical spectroscopic techniques are proven to be extremely sensitive to structural changes.

The analysis of the Drude component of the dielectric function of CoFeB allowed extracting information regarding the resistivity and charge-carrier scattering time, which is closely related to the crystalline order in the films. It was thus possible to identify 450°C as the temperature at which nucleation of CoFe crystallites occurs. Corroborating the results of spectroscopic ellipsometry, SEM and XRD demonstrate that the nucleation of the crystallization starts at the interface between the  $\text{Co}_x\text{Fe}_{(80-x)}\text{B}_{20}$  and the crystalline Pt capping layer.

The magneto-optical off-diagonal component of the dielectric function of  $\text{Co}_x\text{Fe}_{(80-x)}\text{B}_{20}$  extracted from the MOKE

spectra shows significant changes with the composition of the alloy as well as with the amorphous to crystalline structural evolution.

This study underlines the utility of spectroscopic ellipsometry and MOKE spectroscopy for material optimization in the field of metallic alloys for spintronic applications.

## ACKNOWLEDGMENT

This work was supported by the Deutsche Forschungsgemeinschaft (DFG) under the project “Interfacial perpendicular magnetic anisotropy for next-generation monolithic 3D TMR sensors” (Project No. 282193534) and by the Fraunhofer Internal Programmes under Grant No. MEF 836303.

- [1] P. Mohn, *J. Phys. C: Solid State Phys.* **21**, 2841 (1988).
- [2] Y. Bourourou, L. Beldi, B. Bentría, A. Gueddouch, and B. Bouhaf, *J. Magn. Magn. Mater.* **365**, 23 (2014).
- [3] W. Kettler, R. Wernhardt, and M. Rosenberg, *J. Appl. Phys.* **53**, 8248 (1982).
- [4] T. Kawahara, K. Ito, R. Takemura, and H. Ohno, *Microelectron. Reliab.* **52**, 613 (2012).
- [5] P. P. Freitas, R. Ferreira, and S. Cardoso, *Proc. IEEE* **104**, 1894 (2016).
- [6] C. Zheng, K. Zhu, S. Cardoso de Freitas, J.-Y. Chang, J. E. Davies, P. Eames, P. P. Freitas, O. Kazakova, C. Kim, C.-W. Leung, S.-H. Liou, A. Ognev, S. N. Piramanayagam, P. Ripka, A. Samardak, K.-H. Shin, S.-Y. Tong, M.-J. Tung, S. X. Wang, S. Xue, X. Yin, and P. W. T. Pong, *IEEE Trans. Magn.* **55**, 0800130 (2019).
- [7] D. D. Djayaprawira, K. Tsunekawa, M. Nagai, H. Maehara, S. Yamagata, N. Watanabe, S. Yuasa, Y. Suzuki, and K. Ando, *Appl. Phys. Lett.* **86**, 092502 (2005).
- [8] H. Hauser and R. Grössinger, *J. Appl. Phys.* **85**, 5133 (1999).
- [9] S. X. Huang, T. Y. Chen, and C. L. Chien, *Appl. Phys. Lett.* **92**, 242509 (2008).
- [10] C. Bilzer, T. Devolder, J.-V. Kim, G. Counil, C. Chappert, S. Cardoso, and P. P. Freitas, *J. Appl. Phys.* **100**, 053903 (2006).
- [11] T. Devolder, J. V. Kim, L. Nistor, R. Sousa, B. Rodmacq, and B. Diény, *J. Appl. Phys.* **120**, 183902 (2016).
- [12] S. Ikeda, J. Hayakawa, Y. M. Lee, R. Sasaki, T. Meguro, F. Matsukura, and H. Ohno, *Jpn. J. Appl. Phys.* **44**, L1442 (2005).
- [13] S. Ikeda, J. Hayakawa, Y. Ashizawa, Y. M. Lee, K. Miura, H. Hasegawa, M. Tsunoda, F. Matsukura, and H. Ohno, *Appl. Phys. Lett.* **93**, 082508 (2008).
- [14] A. Sharma, M. A. Hoffmann, P. Matthes, S. Busse, O. Selyshchev, P. Mack, H. Exner, A. Horn, S. E. Schulz, D. R. T. Zahn, and G. Salvan, *J. Magn. Magn. Mater.* **489**, 165390 (2019).
- [15] B. Sun, G. Q. Li, W. X. Zhao, Z. Shen, Y. H. Liu, and P. Chen, *Mater. Lett.* **123**, 221 (2014).
- [16] T. Takeuchi, K. Tsunekawa, Y. Choi, Y. Nagamine, D. D. Djayaprawira, A. Genseki, Y. Hoshi, and Y. Kitamoto, *Jpn. J. Appl. Phys.* **46**, L623 (2007).
- [17] S. U. Jen, Y. D. Yao, Y. T. Chen, J. M. Wu, C. C. Lee, T. L. Tsai, and Y. C. Chang, *J. Appl. Phys.* **99**, 053701 (2006).
- [18] S. Cardoso, C. Cavaco, R. Ferreira, L. Pereira, M. Rickart, P. P. Freitas, N. Franco, J. Gouveia, and N. P. Barradas, *J. Appl. Phys.* **97**, 10C916 (2005).
- [19] R. Lavrijsen, P. V. Paluskar, C. T. J. Loermans, P. A. Van Kruisbergen, J. T. Kohlhepp, H. J. M. Swagten, B. Koopmans, and E. Snoeck, *J. Appl. Phys.* **109**, 093905 (2011).
- [20] E. A. Irene, *Thin Solid Films* **233**, 96 (1993).
- [21] M. Wakagi, H. Fujiwara, and R. W. Collins, *Thin Solid Films* **313–314**, 464 (1998).
- [22] J. L. Carvalho, M. E. Somers, and K. Dalnoki-Veress, *J. Polym. Sci. Part B Polym. Phys.* **49**, 712 (2011).
- [23] S. Engmann, V. Turkovic, H. Hoppe, and G. Gobsch, *J. Phys. Chem. C* **117**, 25205 (2013).
- [24] B. Bräuer, M. Fronk, D. Lehmann, D. R. T. Zahn, and G. Salvan, *J. Phys. Chem. B* **113**, 14957 (2009).
- [25] K. K. Tikuišis, L. Beran, P. Cejpek, K. Uhlřřová, J. Hamrle, M. Vaňatka, M. Urbánek, and M. Veis, *Mater. Des.* **114**, 31 (2017).
- [26] K. J. Kim, S. J. J. Lee, and J. M. M. Park, *J. Magn. Magn. Mater.* **241**, 6 (2002).
- [27] K. J. Kim, S. J. Lee, and D. W. Lynch, *Solid State Commun.* **114**, 457 (2000).
- [28] M. Kumar, T. Nautiyal, and S. Auluck, *Eur. Phys. J. B* **73**, 423 (2010).
- [29] X. Liang, X. Xu, R. Zheng, Z. A. Lum, and J. Qiu, *Appl. Opt.* **54**, 1557 (2015).
- [30] A. M. Kalashnikova, V. V. Pavlov, R. V. Pisarev, Y. E. Kalinin, A. V. Sitnikov, and T. Rasing, *Phys. Solid State* **46**, 2163 (2004).
- [31] M. A. Hoffmann, A. Sharma, P. Matthes, S. Okano, O. Hellwig, R. Ecke, D. R. T. Zahn, G. Salvan, and S. E. Schulz, *J. Phys.: Condens. Matter* **32**, 055702 (2020).
- [32] Y. Waseda, E. Matsubara, and K. Shinoda, *X-Ray Diffraction Crystallography* (Springer, Berlin, 2011).
- [33] M. Björck and G. Andersson, *J. Appl. Crystallogr.* **40**, 1174 (2007).
- [34] C. M. Herzinger, B. Johs, W. A. McGahan, J. A. Woollam, and W. Paulson, *J. Appl. Phys.* **83**, 3323 (1998).
- [35] D. W. Lynch and W. R. Hunter, in *Handbook. Opt. Constants Solids*, edited by E. D. Palik (Elsevier, Burlington, 1997), pp. 340–341.
- [36] A. D. Rakić, A. B. Djurišić, J. M. Elazar, and M. L. Majewski, *Appl. Opt.* **37**, 5271 (1998).
- [37] T. Herrmann, K. Lüdge, W. Richter, K. G. Georgarakis, P. Pouloupoulos, R. Nünthel, J. Lindner, M. Wahl, and N. Esser, *Phys. Rev. B* **73**, 134408 (2006).
- [38] J. Zak, E. R. Moog, C. Liu, and S. D. Bader, *Phys. Rev. B* **43**, 6423 (1991).
- [39] A. K. Rumaiz, J. C. Woicik, W. G. Wang, J. Jordan-Sweet, G. H. Jaffari, C. Ni, J. Q. Xiao, and C. L. Chien, *Appl. Phys. Lett.* **96**, 112502 (2010).
- [40] Y. Fuji, S. Kaji, M. Hara, Y. Higashi, A. Hori, K. Okamoto, T. Nagata, S. Baba, A. Yuzawa, K. Otsu, K. Masunishi, T. Ono, and H. Fukuzawa, *Appl. Phys. Lett.* **112**, 062405 (2018).
- [41] O. Hellwig, D. T. Margulies, B. Lengsfeld, E. E. Fullerton, and J. B. Kortright, *Appl. Phys. Lett.* **80**, 1234 (2002).
- [42] D. Li, Y. N. Xu, and W. Y. Ching, *Phys. Rev. B* **45**, 5895 (1992).

- [43] G. Ventrua and L. Risegari, in *The Art of Cryogenics*, first edition (Elsevier Science, eBook, 2008), pp. 89–102.
- [44] J. Babiskin and J. R. Anderson, in *American Institute of Physics Handbook*, third edition (Mc Graw Hill, New York, 1972), p. 204.
- [45] K. Fuchs, *Math. Proc. Cambridge Philos. Soc.* **34**, 100 (1938).
- [46] D. Weller, W. Reim, H. Ebert, D. D. Johnson, and F. J. Pinski, *J. Phys. Colloq.* **49**, C8-41 (1988).
- [47] T. Maurer, J. Sticht, P. M. Oppeneer, F. Herman, and J. Kübler, *J. Magn. Magn. Mater.* **104–107**, 1029 (1992).
- [48] G. S. Krinchik and V. A. Artem'ev, *Zh. Eksp. Teor. Fiz.* **53**, 1901 (1967) [*Sov. Phys. JETP* **26**, 1080 (1968)].
- [49] R. M. Osgood, III, K. T. Riggs, A. E. Johnson, J. E. Mattson, C. H. Sowers, and S. D. Bader, *Phys. Rev. B* **56**, 2627 (1997).
- [50] P. H. Lee, Z. R. Xiao, K. L. Chen, Y. Chen, S. W. Kao, and T. S. Chin, *Phys. B: Condens. Matter* **404**, 1989 (2009).
- [51] A. Y. Liu and D. J. Singh, *Phys. Rev. B* **46**, 11145 (1992).